Computational Approaches for Crack Propagation in Materials and Structures: Comparison Between Linear Elastic Fracture Mechanics (LEFM) and Peridynamics (PD) Based Strategies

Meral Tuna, Greta Ongaro, Patrizia Trovalusci, Nicholas Fantuzzi

Abstract In solid mechanics, the defects and imperfections of materials (e.g., cracks, dislocations, etc.) play a key role on the overall mechanical behaviour of the structure despite their localized character. In this paper, the phenomenon of crack propagation under tension (Mode I) has been investigated considering two different approaches: linear elastic fracture mechanics (LEFM) and bond-based peridynamics (PD). For the former, the progression of crack path is simulated with the aid of extended finite element method (XFEM), which eliminates the need to have conforming mesh with crack geometry by locally enriching the nodes located in the influence domain of discontinuity and singularity. For the latter, a classical continuum mechanics-peridynamics (CCM-PD) coupling strategy is utilized to combine the ability of peridynamics to handle displacement fields discontinuity with the compu-

Meral Tuna
Department of Civil, Chemical, Environmental, and Materials Engineering, University of Bologna, Viale del Risorgimento 2, 40136 Bologna, Italy
e-mail: meral.tunaeroglu@unibo.it
Department of Structural and Geotechnical Engineering, Sapienza University of Rome, v. A. Gramsci 53, 00197 Rome, Italy
e-mail: meral.tunaeroglu@uniroma1.it

Greta Ongaro
Department of Structural and Geotechnical Engineering, Sapienza University of Rome, v. A. Gramsci 53, 00197 Rome, Italy
e-mail: greta.ongaro@uniroma1.it

Patrizia Trovalusci
Department of Structural and Geotechnical Engineering, Sapienza University of Rome, v. A. Gramsci 53, 00197 Rome, Italy
e-mail: patrizia.trovalusci@uniroma1.it

Nicholas Fantuzzi
Department of Civil, Chemical, Environmental, and Materials Engineering, University of Bologna, Viale del Risorgimento 2, 40136 Bologna, Italy
e-mail: nicholas.fantuzzi@unibo.it

tational efficiency of continuum-based modeling approaches. All the formulations are developed within two-dimensional (2D) linearized framework, and implemented through in-house codes. The correspondence between LEFM based XFEM and CCM-PD coupled models is discussed through a benchmark problem of practical importance: a uniaxially deformed finite plate with an edge crack, focusing on the variation of fracture parameters and comparing the computational efficiency of the approaches.

1 Introduction

Fracture refers to new material surface formation in an irreversible manner, which can take place on different scale levels (i.e., from atomistic to continuum), and is generally categorized as brittle (i.e., sudden failure, low energy dissipation) and ductile (i.e., progressive degradation, high energy dissipation) depending on the amount of plastic deformation that occurs at the process zone as a result of either static or dynamic loads.

Understanding fracture mechanism (i.e. initiation/nucleation, propagation/growth, coalescence, resting of cracks) is of vital importance for the reliable application of materials since cracks have a deteriorating effect on the strength of structures, particularly pronounced in brittle (non-ductile) case (Inglis, 1913; Gdoutos, 2006). Given the high costs and time constraints associated with experimental testing, various methods with each one having its own set of advantages and limitations, are exploited. Depending on the principles followed while modeling the structure under investigation, the approaches can be categorized in three different groups as listed below.
(i) Continuum-based: linear elastic fracture mechanics (LEFM) (Griffith, 1921; Irwin, 1968), cohesive zone model (CZM) (Dugdale, 1960; Barenblatt, 1962), nonlocal and gradient-enhanced damage models (DM) (Pijaudier-Cabot and Bažant, 1987; Peerlings et al., 1996; de Borst et al., 1996; Moës et al., 2011), phase field method (PFM) (Francfort and Marigo, 1998; Bourdin et al., 2008; Miehe et al., 2010), peridynamics (PD) (Silling, 2000; Silling and Askari, 2005; Silling et al., 2007),
(ii) Discontinuum-based: discrete element method (DEM) (Cundall and Strack, 1979; Zhao et al., 2022), lattice model (Chiaia et al., 1997; Mariano and Trovalusci, 1999; Topin et al., 2007), particle model (Ostoja-Starzewski and Wang, 2006),
(iii) Partitioned-domain multi-scale: coupled atomistic-continuum models (Tadmor and Miller, 2011), coupled continuum-peridynamics approaches (Shojaei et al., 2016; Galvanetto et al., 2016; Zaccariotto et al., 2018; Chen et al., 2022), etc.

Among those, the linear elastic fracture mechanics (LEFM) and peridynamics (PD), forms the basis of this work following their wide range of appli-

cations in modeling cracked structures, about which a brief literature review is provided in the following subsections.

1.1 Linear Elastic Fracture Mechanics (LEFM)

The foundation of LEFM dates back to Griffith (1921) in which the strength of scratched glass specimens is investigated under uniaxial tension by revealing the inverse relation between rupture stress and crack length for the first time. Accordingly, the crack is suggested to propagate when the rate of potential energy decrease (also known as *strain energy release rate*) equals to or is greater than the rate of the energy consumed/absorbed in the generation of new material surfaces. Here the former part refers to *driving force*, whereas the latter part, which quantifies the disruption of the bonds, is a material property defining the *resistance force*. The *Griffith's theory* was later extended by Irwin (1948) and Orowan (1949) to cover the effect of plastic dissipation that is confined to a very small process zone adjacent to the crack front as in quasi-brittle materials. The establishment of the concept of *stress intensity factor* (SIF), which expresses the amplitude of stress singularity at the crack tip, and displaying its connection with *energy release rate* (ERR), allowed utilization of the near crack tip local fields to study the response of cracked materials (Irwin, 1957). Moreover, the basic fracture parameters (e.g., near crack-tip stress and displacement fields, crack opening displacement, SIF, ERR) describes the damage characteristics of the structures under investigation by treating any loading state as a combination of Mode I (opening), Mode II (shearing) and Mode III (tearing) cases. These parameters, that can be determined experimentally, analytically or numerically (e.g., finite element method (FEM), extended finite element method (XFEM), boundary element method (BEM), virtuel element method (VEM), meshless methods (MM)) with the aid of path independent line or domain integrals; *J-integral*, *I-integral* (Cherepanov, 1967; Rice, 1968; Eshelby, 1974; Stern et al., 1976; Moran and Shih, 1987), are then substituted into employed fracture criterion (e.g., the maximum tangential/circumferential stress (Erdogan and Sih, 1963; Smith et al., 2006), the minimum strain energy density (Sih, 1974; Ayatollahi et al., 2015), the maximum energy release rate (Hussain et al., 1973; Nuismer, 1975; Hou et al., 2019), etc.) in order to predict the direction of crack propagation. At this point, it should be mentioned that the most criteria endorse each other in the case of Mode I, yet deviate under Mode II dominated loading conditions. In such a case, the discrepancy is attributed to the omission of higher order terms, hence the inconsistency between theoretical predictions and experimental results are claimed to be alleviated by generalizing the calculations via including the non-singular terms. Nevertheless, as the focus herein is on the Mode I case, further details related to Mode II dominated loading conditions are avoided. As in LEFM, it is essential to

obtain the basic fracture parameters, the present study conducts extended finite element method (XFEM), that is developed by Belytschko and Black (1999); Dolbow (1999); Moes et al. (1999); Daux et al. (2000) following its efficiency in modeling the discontinuities without the need to have conforming mesh with crack geometry and/or material interface (Sukumar and Prevost, 2003; Huang et al., 2003).

1.2 Peridynamics (PD) and local-to-nonlocal coupling

Peridynamics (PD) theory was proposed by Silling (2000) and later extended, culminating in its final form referred to as state-based version, as detailed in Silling et al. (2007). The theory emerges as a nonlocal reformulation of classical continuum mechanics (CCM) in which the body is assumed to be comprised of material points capable of interacting within a finite distance, referred to as *horizon*. The *horizon* represents the region where nonlocal interactions occur hence serves as a characteristic length scale (Bobaru and Hu, 2012). As the theory relies on integro-differential equations, the equation of motion is defined by replacing the divergence of the stress tensor with an integral operator. This makes the governing equations of PD to be applicable even in the presence of discontinuous displacement fields allowing for the natural treatment of fracture and failure as material responses (Silling, 2000; Bobaru et al., 2016) without necessitating predefined criteria for crack propagation phenomenon (Ongaro et al., 2021). The distinctive features of PD leads to a surge in the exploration and implementation of innovative computational methods grounded on it for analyzing different materials (Hu et al., 2012; Zhu et al., 2016; Hermann et al., 2022; Sheikhbahaei et al., 2023) across various length scales, from macro to nanoscales (Askari et al., 2008; Ongaro et al., 2022, 2023a). Nevertheless, despite its efficiency PD model comes with a computational cost due to its nonlocal nature, which leads to computationally expensive analysis compared to CCM-based approaches (Bobaru et al., 2016), hence impedes its application in large-scale, geometrically complex simulations (Shojaei et al., 2020). Moreover, PD numerical implementations encounter challenges related to nonlocal boundary conditions (Silling, 2000), where boundaries appear fuzzy, requiring displacement or load conditions to be imposed in finite volumetric regions rather than on boundary surfaces (Aksoylu and Parks, 2011; Seleson et al., 2013b; Scabbia et al., 2021, 2023). Another aspect to consider is the so called surface effect, which is related to the emergence of spurious effects near the boundary of a finite domain due to assumptions made for material points close to the boundary and that impact the numerical solution of PD models (Ha and Bobaru, 2011; Le and Bobaru, 2018). To address these challenges, it becomes advantageous to explore the coupling of PD and CCM models, leveraging the strengths of both

models while mitigating their respective drawbacks (Galvanetto et al., 2016; Zaccariotto et al., 2018, 2021; Ongaro et al., 2021).

In the coupling of CCM and PD, it is customary to describe small regions within a domain, potentially impacted by the presence of discontinuities, using a PD model. The remaining portions of the domain are then efficiently represented through a CCM model (Galvanetto et al., 2016; Zaccariotto et al., 2018, 2021; Ongaro et al., 2021). Specifically, a common approach involves coupling PD models based on the meshfree discretization outlined in Silling and Askari (2005) with CCM models discretized using the FEM. Extensive research efforts have been devoted to the investigation of local-to-nonlocal coupling, with a significant focus on coupling CCM and PD models (Macek and Silling, 2007; D'Elia et al., 2021; Ongaro et al., 2021). This has led to the development of various techniques, including optimization-based (D'Elia and Bochev, 2015, 2021), partitioned (Yu et al., 2018; You et al., 2020), Arlequin (Han and Lubineau, 2012), morphing (Lubineau et al., 2012; Han et al., 2016), quasi-nonlocal (Jiang and Shen, 2022), blending (Seleson et al., 2013a, 2015), splice (Silling et al., 2015), variable horizon (Silling et al., 2015), and partial stress (Silling et al., 2015) methods, while in this work, our focus is on the coupling technique proposed in a series of papers (Shojaei et al., 2016; Galvanetto et al., 2016; Shojaei et al., 2017; Zaccariotto et al., 2018), that can be regarded as an application of the splice method.

The study is organized as follows. In the first part of Section 2, the XFEM formulation, derived within the linearized kinematical framework under plane strain assumption considering isotropy, is presented in a detailed way to ensure the reproducibility of the results. In the second part, an overview of the bond-based version of PD theory and its discretization is provided together with a brief description of the CCM-PD coupling strategy exploited in the present work. In Section 3, with the aid of in-house codes, developed in Wolfram Mathematica and Matlab-Mathworks environments, for XFEM and CCM-PD coupled models, respectively, a parametric study is performed regarding a finite plate with an edge crack. The variation of crack mouth opening displacement and axial force are investigated while the domain is subjected to a prescribed uniform vertical displacement promoting crack opening (Mode I fracture). In Section 4, the study is concluded by comparing the results of the two approaches with a focus on their computational efficiency according to which future developments are suggested.

2 Material and Methods

In the first part of this section, the basics of XFEM are summarized for two-dimensional (2D) cases under plane strain assumption, while, in the second part, the PD theory is briefly outlined together with an overview of the key features of the CCM-PD coupling strategy exploited to study 2D systems un-

der plane strain conditions. Here the PD model is given by a two-dimensional linear bond-based isotropic model (Silling, 2000, 2010), while in both approaches, the formulations for classical continuum parts are presented for linearized kinematical framework by considering the domain as elastic, homogeneous, and isotropic. For the classical continuum parts, the models are uniformly discretized with 4-node (linear) quadrilateral extended and standard finite elements, while, for the PD portion, the model is uniformly discretized employing the meshfree standard discretization scheme (Silling and Askari, 2005). The formulations are implemented through in-house codes built in Wolfram Mathematica and Matlab-Mathworks environments, for XFEM and CCM-PD coupled models, respectively.

2.1 Extended Finite Element Method (XFEM)

XFEM (Belytschko and Black, 1999; Dolbow, 1999; Moes et al., 1999; Daux et al., 2000) is an efficient numerical tool for modeling discontinuities without the need to have conforming mesh with crack geometry and/or material interface (Sukumar and Prevost, 2003; Huang et al., 2003) by locally enriching the nodes located in the influence domain of discontinuity and/or singularity through adding special functions in the standard FE approximation field(s). As in this case only the homogenized medium is considered, the nodes of element(s), that entirely split by crack and containing crack tip(s), are endowed with Heaviside-step and crack-tip related degrees of freedom (DOFs) respectively, which is illustrated in Fig. 1 considering a straight crack.

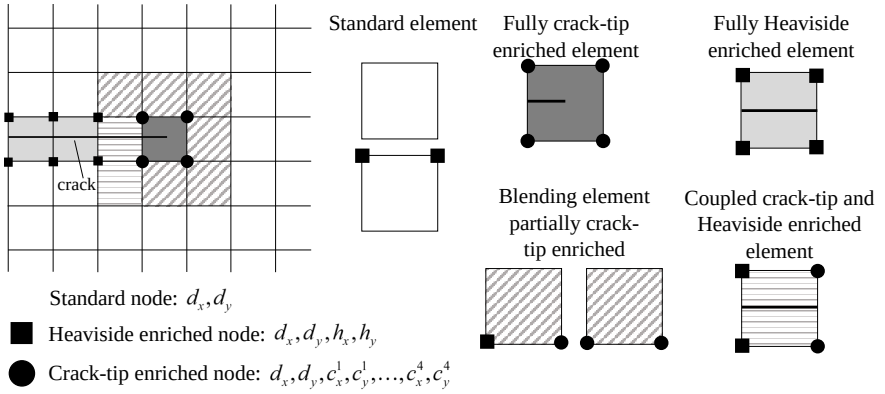

Fig. 1: The element and node types in extended finite element method illustrated through a domain with straight crack.

As well known, Heaviside step function, $H(\mathbf{x})$, is used in modeling the strong discontinuity across the element that is caused by the crack split where $\mathbf{x}$ is the global Cartesian coordinate of the point under investigation which could either be node or Gauss sampling point. Basically, for points above and below the crack, Heaviside function takes the values of +1 and -1, respectively with having a discontinuity at the interface, which allows simulation of the crack partition:

$$H(\mathbf{x}) = \left\{ \begin{array}{l} +1 \text{ if } (\mathbf{x} - \mathbf{x}^*) . \mathbf{n} > 0 \\ -1 \text{ otherwise} \end{array} \right\}. \tag{1}$$

Here $\mathbf{x}^*$ lies on the crack face and refers to the coordinate of the closest point to $\mathbf{x}$ with a unit normal vector $\mathbf{n}$. Meanwhile, crack tip enrichment functions, $\mathbf{\Phi}(\mathbf{r})$, are used to model the singularity around the crack tip in an efficient manner by mimicking the asymptotic behaviour of displacement field with $\mathbf{r}$ referring to the local polar coordinates of the point (r, θ). Accordingly, the branch functions obtained for the near crack-tip asymptotic fields are used to cover the singularity (Fleming et al., 1997):

$$\begin{aligned} \mathbf{\Phi}(\mathbf{r}) &= \left\{ \Phi^1, \Phi^2, \Phi^3, \Phi^4 \right\} \\ &= \left\{ \sqrt{r}\mathrm{Sin}\frac{\theta}{2},\ \sqrt{r}\mathrm{Cos}\frac{\theta}{2},\ \sqrt{r}\mathrm{Sin}\frac{\theta}{2}\mathrm{Sin}\theta,\ \sqrt{r}\mathrm{Cos}\frac{\theta}{2}\mathrm{Sin}\theta \right\}. \end{aligned} \tag{2}$$

As the current form of Heaviside step and crack-tip branch functions lead to violation of Kronecker-δ property, the formulation is modified through the shifting functions:

$$H(\mathbf{x}) - \bar{H}(\mathbf{x}_i),\ \mathbf{\Phi}(\mathbf{r}) - \bar{\mathbf{\Phi}}(\mathbf{r}_i), \quad i = 1, \ldots, 4 \tag{3}$$

where $\bar{H}(\mathbf{x}_i)$ and $\bar{\mathbf{\Phi}}(\mathbf{r}_i)$ refer to values of Heaviside-step and crack-tip branch functions at ith node of the element.

Before moving to the formulation, the formation of the lists including the node sets for enrichment should be explained. First, the nodes of element(s) that contains the crack tip(s) is enriched with branch functions. In this case, the number of nodes can be increased via fixed enrichment area scheme, which is proposed by Laborde et al. (2005) to avoid mesh dependency for very fine discretization. Second, the nodes of element(s) that is intersected by the crack is enriched with the step function while following exceptions must be kept in mind. For instance, the node(s) that belong to the element(s) containing the crack-tip(s) must be excluded as the discontinuity has already been accounted for through the first branch function. Moreover, one needs to pay attention to the ratio between partitioned areas and support domain of the Heaviside enriched node, as lower values result in ill-conditioned stiffness matrices (Moes et al., 1999; Daux et al., 2000), where the total area of the elements containing the corresponding node, and split into two parts (i.e., partitioned areas) by the crack, is known as support domain. For the present study, this

condition is automatically satisfied as crack always cuts the elements into two equal pieces.

2.1.1 Standard element

The standard formulation is employed for the elements that do not contain any enriched node or for those that contain only Heaviside enriched node but not split by crack as illustrated in Fig. 1. The latter case can be justified through the fact that $H(\mathbf{x}) - \bar{H}(\mathbf{x}_i)$ equals to zero hence vanishes when the element is located above or below the crack. Accordingly, for a standard element m, the nodal unknown vector including the displacement related DOFs of nodes along horizontal and vertical axes; d_x and d_y takes the following form as seen from Fig. 2(**a**):

$$\mathbf{d}_m = \left\{ d_{x_1}\ d_{y_1}\ \ldots\ d_{x_4}\ d_{y_4} \right\}_m^{\mathrm{T}}. \tag{4}$$

where subscripts from 1 to 4 refers to node number. The approximate displacement field, $\mathbf{u}_m$, is calculated as:

$$\begin{aligned} &\mathbf{u}_m = \mathbf{N}(\boldsymbol{\xi})\,\mathbf{d}_m, \\ &\begin{Bmatrix} u_1 \\ u_2 \end{Bmatrix}_m = \begin{bmatrix} N_1(\boldsymbol{\xi}) & 0 & \cdots & N_4(\boldsymbol{\xi}) & 0 \\ 0 & N_1(\boldsymbol{\xi}) & \cdots & 0 & N_4(\boldsymbol{\xi}) \end{bmatrix} \begin{Bmatrix} d_{x_1} \\ d_{y_1} \\ \vdots \\ d_{x_4} \\ d_{y_4} \end{Bmatrix}_m, \end{aligned} \tag{5}$$

with the aid of linear shape functions, represented in terms of natural coordinates; $\boldsymbol{\xi} = \{\xi, \eta\} \in [-1, +1]$:

$$\begin{aligned} N_1(\boldsymbol{\xi}) &= \frac{(1-\xi)(1-\eta)}{4}, \quad N_2(\boldsymbol{\xi}) = \frac{(1+\xi)(1-\eta)}{4}, \\ N_3(\boldsymbol{\xi}) &= \frac{(1+\xi)(1+\eta)}{4}, \quad N_4(\boldsymbol{\xi}) = \frac{(1-\xi)(1+\eta)}{4}. \end{aligned} \tag{6}$$

In such a case, the corresponding strain field is calculated as

$$\boldsymbol{\varepsilon}_m^{\mathrm{std}} = \mathbf{L}_m \mathbf{u}_m = \mathbf{B}_m^{\mathrm{std}} \mathbf{d}_m, \tag{7}$$

where $\mathbf{L}_m$ refers to differential operator

$$\mathbf{L}_m = \begin{bmatrix} \dfrac{\partial}{\partial x_1} & 0 \\ 0 & \dfrac{\partial}{\partial x_2} \\ \dfrac{\partial}{\partial x_2} & \dfrac{\partial}{\partial x_1} \end{bmatrix} = \begin{bmatrix} \dfrac{\partial}{\partial \xi} J_{11}^{\mathrm{GN}} + \dfrac{\partial}{\partial \eta} J_{21}^{\mathrm{GN}} & 0 \\ 0 & \dfrac{\partial}{\partial \xi} J_{12}^{\mathrm{GN}} + \dfrac{\partial}{\partial \eta} J_{22}^{\mathrm{GN}} \\ \dfrac{\partial}{\partial \xi} J_{12}^{\mathrm{GN}} + \dfrac{\partial}{\partial \eta} J_{22}^{\mathrm{GN}} & \dfrac{\partial}{\partial \xi} J_{11}^{\mathrm{GN}} + \dfrac{\partial}{\partial \eta} J_{21}^{\mathrm{GN}} \end{bmatrix}_m , \quad (8)$$

and $\mathbf{B}_m^{\mathrm{std}}$ is the strain matrix including the derivatives of shape functions with respect to global coordinates; $\mathbf{x} = (x_1, x_2)$:

$$\mathbf{B}_m^{\mathrm{std}} = \mathbf{L}_m \mathbf{N}(\boldsymbol{\xi}) . \quad (9)$$

As this procedure requires the use of chain rule, the inverse of Jacobian matrix $\mathbf{J}_m^{\mathrm{NG}}$, that gives the direct mapping between natural (N) and global (G) coordinates is utilized:

$$\mathbf{J}_m^{\mathrm{NG}^{-1}} = \mathbf{J}_m^{\mathrm{GN}} = \begin{bmatrix} J_{11}^{\mathrm{GN}} & J_{12}^{\mathrm{GN}} \\ J_{21}^{\mathrm{GN}} & J_{22}^{\mathrm{GN}} \end{bmatrix}_m = \begin{bmatrix} \dfrac{\partial x_1(\boldsymbol{\xi})}{\partial \xi} & \dfrac{\partial x_1(\boldsymbol{\xi})}{\partial \eta} \\ \dfrac{\partial x_2(\boldsymbol{\xi})}{\partial \xi} & \dfrac{\partial x_2(\boldsymbol{\xi})}{\partial \eta} \end{bmatrix}_m^{-1} , \quad (10)$$

where $x_1(\boldsymbol{\xi})$ and $x_2(\boldsymbol{\xi})$ are the components of coordinate vector for an element m with x_{1_i} and x_{2_i} referring to physical coordinates of node i:

$$x_1(\boldsymbol{\xi}) = \sum_{i=1}^{4} N_i(\boldsymbol{\xi}) x_{1_i}, \quad x_2(\boldsymbol{\xi}) = \sum_{i=1}^{4} N_i(\boldsymbol{\xi}) x_{2_i}. \quad (11)$$

Finally, the stiffness matrix of a standard element m takes the form:

$$\mathbf{k}_m^{\mathrm{std}} = h \int_{-1}^{+1} \int_{-1}^{+1} \mathbf{B}_m^{\mathrm{std}^{\mathrm{T}}} \mathbf{D} \mathbf{B}_m^{\mathrm{std}} \left| \mathbf{J}_m^{\mathrm{NG}} \right| \mathrm{d}\xi \mathrm{d}\eta, \quad (12)$$

with following element formulation;

$$\mathbf{f}_m^{\mathrm{std}} = \mathbf{k}_m^{\mathrm{std}} \mathbf{d}_m. \quad (13)$$

Here $\mathbf{f}_m^{\mathrm{std}}$ is the standard load vector and $\mathbf{D}$ is the elasticity matrix which takes the below-given form for plane strain assumption:

$$\mathbf{D} = \begin{bmatrix} \lambda + 2\mu & \lambda & 0 \\ \lambda & \lambda + 2\mu & 0 \\ 0 & 0 & \mu \end{bmatrix}, \quad (14)$$

where λ and μ are the Lame's constants.

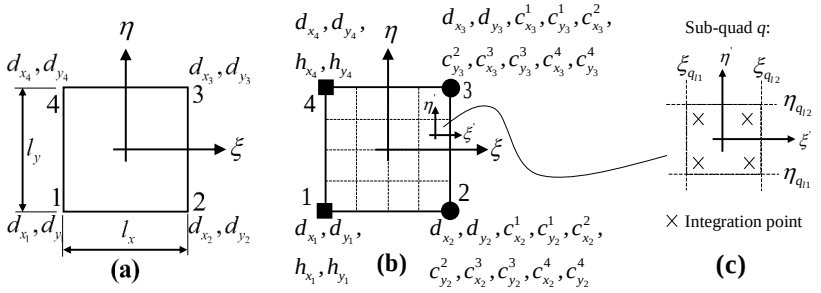

Fig. 2: (**a**) Standard element, (**b**) coupled enriched element with corresponding sub-quads, $n_{\text{sub}} = 16$, required for numerical integration, (**c**) zoom-in look of a sub-quad.

2.1.2 Enriched element

Heaviside, $\mathbf{k}_m^{\text{hvs}}$, and crack-tip, $\mathbf{k}_m^{\text{ctp}}$, enriched formulations are required for the element(s) that are completely split by crack and for those having at least one crack-tip enriched node. In such a case, new nodal unknown vectors, $\mathbf{h}_m$ and $\mathbf{c}_m$ are emerged, in addition to the standard one $\mathbf{d}_m$:

$$\begin{aligned} \mathbf{h}_m &= \left\{ h_{x_1}\ h_{y_1}\ \dots\ h_{x_4}\ h_{y_4} \right\}_m^{\mathrm{T}}, \\ \mathbf{c}_m &= \left\{ c_{x_1}^1\ c_{y_1}^1\ \dots\ c_{y_1}^4\ \dots\ c_{x_4}^1\ c_{y_4}^1\ \dots\ c_{y_4}^4 \right\}_m^{\mathrm{T}}. \end{aligned} \tag{15}$$

Here the former is related to Heaviside enrichment and has the same dimensions as the standard nodal unknown vector for a fully endowed element. The latter, on the other hand, corresponds to the crack-tip enrichment for which each enriched node possesses eight DOFs (four per each translational DOF following four branch functions) where superscript from 1 to 4 refers to branch functions. It should be reminded that, as this study does not account for fixed area enrichment scheme, each node can be endowed either with heaviside or crack-tip related DOFs. Hence for an enriched element m, $\mathcal{N}_m^H$ and $\mathcal{N}_m^C$ give the lists of nodes associated with Heaviside and crack-tip enrichments, respectively. Following this fact, one could define the corresponding shape function matrices in a more convenient manner:

$$\mathbf{N}_m^{\text{hvs}} = \begin{bmatrix} N_I(\xi)\left(H(\mathbf{x}) - \bar{H}(\mathbf{x}_I)\right) & 0 \\ 0 & N_I(\xi)\left(H(\mathbf{x}) - \bar{H}(\mathbf{x}_I)\right)\ \cdots \end{bmatrix}_{2\times 2H} \quad I \in \mathcal{N}_m^H, \tag{16}$$

and

$$\mathbf{N}_m^{\text{ctp}} = \begin{bmatrix} N_J(\xi)\left(\Phi^1(\mathbf{r}) - \bar{\Phi}^1(\mathbf{r}_J)\right) & 0 \\ 0 & \cdots\ N_J(\xi)\left(\Phi^4(\mathbf{r}) - \bar{\Phi}^4(\mathbf{r}_J)\right)\ \cdots \end{bmatrix}_{2\times 8C} \quad J \in \mathcal{N}_m^C, \tag{17}$$

where H and C are the number of nodes in sets $\mathcal{N}_m^H$ and $\mathcal{N}_m^C$, respectively. Thereupon, the approximate displacement field within an element m takes the following form:

$$\mathbf{u}_m = \mathbf{N}\left(\boldsymbol{\xi}\right)\mathbf{d}_m^u + \mathbf{N}_m^{\mathrm{hvs}}\left(\boldsymbol{\xi}\right)\mathbf{h}_m + \mathbf{N}_m^{\mathrm{ctp}}\left(\boldsymbol{\xi},\mathbf{r}\right)\mathbf{c}_m, \tag{18}$$

for which the explicit expressions of second and third terms are;

$$\begin{aligned}
\mathbf{N}_m^{\mathrm{hvs}}\left(\boldsymbol{\xi}\right)\mathbf{h}_m &= \sum_{I\in\mathcal{N}_m^H} N_I\left(\boldsymbol{\xi}\right)\left(H\left(\mathbf{x}\right)-\bar{H}\left(\mathbf{x}_I\right)\right)\left\{\begin{array}{c} h_{x_I} \\ h_{y_I}\end{array}\right\}_m, \\
\mathbf{N}_m^{\mathrm{ctp}}\left(\boldsymbol{\xi},\mathbf{r}\right)\mathbf{c}_m &= \sum_{J\in\mathcal{N}_m^C}\sum_{f=1}^{4} N_J\left(\boldsymbol{\xi}\right)\left(\Phi^f\left(\mathbf{r}\right)-\bar{\Phi}^f\left(\mathbf{r}_J\right)\right)\left\{\begin{array}{c} c_{x_J}^f \\ c_{y_J}^f\end{array}\right\}_m.
\end{aligned} \tag{19}$$

Accordingly, for an endowed element, the strain field is written as

$$\varepsilon_m^{\mathrm{std}} = \mathbf{B}_m^{\mathrm{std}}\mathbf{d}_m + \mathbf{B}_m^{\mathrm{hvs}}\mathbf{h}_m + \mathbf{B}_m^{\mathrm{ctp}}\mathbf{c}_m, \tag{20}$$

where the strain matrices, $\mathbf{B}_m^{\mathrm{hvs}}$, $\mathbf{B}_m^{\mathrm{ctp}}$, include the derivatives of shape, Heaviside and branch functions owing to differential operator matrix $\mathbf{L}_m$.

$$\mathbf{B}_m^{\mathrm{hvs}} = \mathbf{L}_m\mathbf{N}_m^{\mathrm{hvs}}\left(\boldsymbol{\xi}\right),\ \mathbf{B}_m^{\mathrm{ctp}} = \mathbf{L}_m\mathbf{N}_m^{\mathrm{ctp}}\left(\boldsymbol{\xi},\mathbf{r}\right). \tag{21}$$

Hence, considering Eq. (19), one needs to perform following differentiation operations:

$$\begin{aligned}
&\frac{\partial N_I\left(\boldsymbol{\xi}\right)}{\partial x_j}\left(H\left(\mathbf{x}\right)-\bar{H}\left(\mathbf{x}_I\right)\right)+\frac{\partial H\left(\mathbf{x}\right)}{\partial x_j}N_I\left(\boldsymbol{\xi}\right), \\
&\frac{\partial N_J\left(\boldsymbol{\xi}\right)}{\partial x_j}\left(\Phi^f\left(\mathbf{r}\right)-\bar{\Phi}^f\left(\mathbf{r}_J\right)\right)+\frac{\partial \Phi^f\left(\mathbf{r}\right)}{\partial x_j}N_J\left(\boldsymbol{\xi}\right),
\end{aligned} \qquad j=1,2 \tag{22}$$

for which chain rule must be utilized with j varying from 1 to 2:

$$\begin{aligned}
\frac{\partial H\left(\mathbf{x}\right)}{\partial x_j} &= \delta\left(\mathbf{x}\right) = \left\{\begin{array}{cc} \infty & \mathbf{x}\text{ on the crack} \\ 0 & \text{other}\end{array}\right\}, \\
\frac{\partial \Phi^f\left(\mathbf{r}\right)}{\partial x_j} &= \left(\frac{\partial \Phi^f\left(\mathbf{r}\right)}{\partial r}J_{11}^{\mathrm{LP}}+\frac{\partial \Phi^f\left(\mathbf{r}\right)}{\partial \theta}J_{21}^{\mathrm{LP}}\right)J_{1j}^{\mathrm{GL}} \\
&\quad+\left(\frac{\partial \Phi^f\left(\mathbf{r}\right)}{\partial r}J_{12}^{\mathrm{LP}}+\frac{\partial \Phi^f\left(\mathbf{r}\right)}{\partial \theta}J_{22}^{\mathrm{LP}}\right)J_{2j}^{\mathrm{GL}}.
\end{aligned} \tag{23}$$

Here $\delta\left(\mathbf{x}\right)$ denotes Dirac delta function which is zero everywhere except for crack interface, hence vanishes as the elemental integration operations will be performed on Gauss points. Moreover $\mathbf{J}^{\mathrm{GL}}$ and $\mathbf{J}^{\mathrm{LP}}$ are the well-known matrices, used for transformation between global Cartesian (G) - local Cartesian (L) and local Cartesian (L) - local polar (P) coordinate systems, respectively:

$$\mathbf{J}^{\mathrm{GL}} = \begin{bmatrix} J_{11}^{\mathrm{GL}} & J_{12}^{\mathrm{GL}} \\ J_{21}^{\mathrm{GL}} & J_{22}^{\mathrm{GL}} \end{bmatrix} = \begin{bmatrix} \dfrac{\partial \tilde{x}_1}{\partial x_1} & \dfrac{\partial \tilde{x}_1}{\partial x_2} \\ \dfrac{\partial \tilde{x}_2}{\partial x_1} & \dfrac{\partial \tilde{x}_2}{\partial x_2} \end{bmatrix} = \begin{bmatrix} \cos\alpha & \sin\alpha \\ -\sin\alpha & \cos\alpha \end{bmatrix},$$
$$\mathbf{J}^{\mathrm{LP}} = \begin{bmatrix} J_{11}^{\mathrm{LP}} & J_{12}^{\mathrm{LP}} \\ J_{21}^{\mathrm{LP}} & J_{22}^{\mathrm{LP}} \end{bmatrix} = \begin{bmatrix} \dfrac{\partial \tilde{x}_1}{\partial r} & \dfrac{\partial \tilde{x}_1}{\partial \theta} \\ \dfrac{\partial \tilde{x}_2}{\partial r} & \dfrac{\partial \tilde{x}_2}{\partial \theta} \end{bmatrix}^{-1} = \begin{bmatrix} \cos\theta & -r\sin\theta \\ \sin\theta & r\cos\theta \end{bmatrix}^{-1}, \tag{24}$$

where α refers to counter-clockwise angle from global horizontal (x_1) to local horizontal ($\tilde{x}_1$) axes.

Consequently, considering the most general case, the element formulation consists of six different sub matrices:

$$\begin{Bmatrix} \mathbf{f}_m^{\mathrm{std}} \\ \mathbf{f}_m^{\mathrm{hvs}} \\ \mathbf{f}_m^{\mathrm{ctp}} \end{Bmatrix} = \begin{bmatrix} \mathbf{k}_m^{\mathrm{std-std}} & \mathbf{k}_m^{\mathrm{std-hvs}} & \mathbf{k}_m^{\mathrm{std-ctp}} \\ \mathbf{k}_m^{\mathrm{hvs-std}} & \mathbf{k}_m^{\mathrm{hvs-hvs}} & \mathbf{k}_m^{\mathrm{hvs-ctp}} \\ \mathbf{k}_m^{\mathrm{std-hvs}} & \mathbf{k}_m^{\mathrm{ctp-hvs}} & \mathbf{k}_m^{\mathrm{ctp-ctp}} \end{bmatrix} \begin{Bmatrix} \mathbf{d}_m \\ \mathbf{h}_m \\ \mathbf{c}_m \end{Bmatrix}, \tag{25}$$

with

$$\mathbf{k}_m^{\mathrm{a-b}} = h \int_{-1}^{+1} \int_{-1}^{+1} \mathbf{B}_m^{\mathrm{a}^{\mathrm{T}}} \mathbf{D} \mathbf{B}_m^{\mathrm{b}} \left|\mathbf{J}_m^{\mathrm{NG}}\right| \mathrm{d}\xi \mathrm{d}\eta, \qquad \mathrm{a,b} : \mathrm{std, hvs, ctp}, \tag{26}$$

while it is clear that $\mathbf{k}_m^{\mathrm{a-b}} = \mathbf{k}_m^{\mathrm{b-a}^{\mathrm{T}}}$.

2.1.3 Extraction of fracture parameters

Within the framework of LEFM, SIFs (the amplitude of stress singularity at the crack-tip), ERR (the strain energy release rate) and COD (the Eucledian distance between the crack surfaces at the tip) are generally considered as basic fracture parameters, that are later implemented into the developed fracture criterion to answer the fundamental question of *"When and along which direction the crack starts to propagate?"*.

In XFEM, the SIFs are generally extracted using the domain form of *interaction integral* (*I-integral*) (Chen and Shield, 1977; Yau et al., 1980), exploiting following equality between SIFs (K_I, K_{II}) and *I-integral*:

$$I = \sum_{s \in \mathcal{N}^I} \int_{-1}^{+1} \int_{-1}^{+1} F_s\left(\xi_{q_p}, \eta_{q_r}\right) \mathrm{q}_{,\tilde{i}} \left|\mathbf{J}^{\mathrm{GL}}\right| \left|\mathbf{J}_s^{\mathrm{NG}}\right| \mathrm{d}\xi \mathrm{d}\eta = \frac{2\left(1-\nu^2\right)}{E} \left(K_I K_I^a + K_{II} K_{II}^a\right), \tag{27}$$

with F_s being;

$$F_s\left(\xi_{q_p}, \eta_{q_r}\right) = \tilde{\sigma}_{ij}^a \tilde{u}_{j,\tilde{1}} + \tilde{\sigma}_{ij} \tilde{u}_{j,\tilde{1}}^a - \tilde{\sigma}_{mn}^a \tilde{\varepsilon}_{mn} \delta_{i1}, \tag{28}$$

where $\mathcal{N}^I$ contains the lists of the elements that are cut by the domain circle centered at the crack tip with a radius of r_I, while the smooth weight function q, is defined as:

$$q\left(\xi\right)=\sum_{i=1}^{4}N_i\left(\xi\right)q_i \qquad \begin{array}{l} q_i=1 \text{ for nodes inside the circle,} \\ q_i=0 \text{ for nodes outside the circle.} \end{array} \tag{29}$$

As previously mentioned, the over tilde symbol denotes that, the stress $\tilde{\sigma}$, strain $\tilde{\epsilon}$ and displacement $\tilde{\mathbf{u}}$ fields and corresponding derivatives are represented in terms of crack-tip local Cartesian coordinate system, while the superscript a indicating the *auxiliary* state. As different from the real state, which is calculated through nodal displacements, the *auxiliary* state is obtained from the analytical expression of near crack-tip fields (Sun and Jin, 2012):

$$\begin{aligned} u_1^a &= \sqrt{\frac{r}{2\pi}}\left(\frac{K_I^a}{2\mu}\cos\frac{\theta}{2}\left(3-4\nu-\mathrm{Cos}\theta\right)+\frac{K_{II}^a}{2\mu}\sin\frac{\theta}{2}\left(5-4\nu+\mathrm{Cos}\theta\right)\right), \\ u_2^a &= \sqrt{\frac{r}{2\pi}}\left(\frac{K_I^a}{2\mu}\sin\frac{\theta}{2}\left(3-4\nu-\mathrm{Cos}\theta\right)+\frac{K_{II}^a}{2\mu}\cos\frac{\theta}{2}\left(4\nu-1-\mathrm{Cos}\theta\right)\right). \end{aligned} \tag{30}$$

Here K_I^a and K_{II}^a are the auxiliary SIFs for Mode I and II, which take the values of either unity or zero to extract the real ones using below-given relations:

$$K_I=\frac{I^{(I)}E}{2\left(1-\nu^2\right)},\; K_{II}=\frac{I^{(II)}E}{2\left(1-\nu^2\right)}, \tag{31}$$

where $I^{(I)}=I\left(K_I^a=1,K_{II}^a=0\right)$ and $I^{(II)}=I\left(K_I^a=0,K_{II}^a=1\right)$.

Meanwhile, the ERR, denoted by G is obtained through *J-integral* (Stern et al., 1976) considering the equality in-between; $J=G$, for which *J-integral* can be calculated either by substituting the extracted values of SIFs into the following relation:

$$J=\frac{1-\nu^2}{E}\left(K_I^2+K_{II}^2\right), \tag{32}$$

or through its definition:

$$J=\sum_{s\in\mathcal{N}^I}J_s=\int_{-1}^{+1}\int_{-1}^{+1}\left(\tilde{\sigma}_{ij}\tilde{u}_{j,\tilde{1}}-\tilde{\sigma}_{mn}\tilde{\varepsilon}_{mn}\delta_{i1}\right)_s \mathrm{q}_{,\tilde{i}}\left|\mathbf{J}^{\mathrm{GL}}\right|\left|\mathbf{J}_s^{\mathrm{NG}}\right|\mathrm{d}\xi\mathrm{d}\eta. \tag{33}$$

2.1.4 Numerical integration

One of the main challenges in XFEM arises during calculation of integrals as endowed elements include discontinuous and singular basis functions. Since in such a case employing Gauss quadrature rule over the whole element will

cause substantial loss in accuracy, Dolbow (1999) proposed the sub-division approach (dividing elements into sub-quads or sub-triangles). This method allows the numerical integrations to be performed separately for smaller portions in the elements where the integrands can still be considered as continuous polynomials. Following its ease at implementation, present study utilizes sub-quads for division (Fig. 1**(b)**) with 2×2 Gauss sampling points (Fig. 1**(c)**). Accordingly, for an enriched element divided into n_{sub} sub-quads, one can calculate stiffness matrix as follows:

$$\mathbf{k}_m^{\text{a-b}} = \sum_{q=1}^{n_{\text{sub}}} \sum_{p=1}^{2} \sum_{r=1}^{2} h \mathbf{B}_m^{\text{a}^{\text{T}}} \left(\xi_{q_p}, \eta_{q_r}\right) \mathbf{D} \mathbf{B}_m^{\text{b}} \left(\xi_{q_p}, \eta_{q_r}\right) \left|\mathbf{J}_m^{\text{NG}}\right| w_{q_p} w_{q_r}, \tag{34}$$

with ξ_{q_p}, η_{q_r}, w_{q_p} and w_{q_r} being the components of $\boldsymbol{\xi}_q, \boldsymbol{\eta}_q$ and $\boldsymbol{w}_q$ vectors, that includes natural coordinates and weights of Gauss sampling points in the sub quad q:

$$\begin{aligned} \boldsymbol{\xi}_q &= \frac{\xi_{ql2} - \xi_{ql1}}{2} \begin{Bmatrix} +1/\sqrt{3} \\ -1/\sqrt{3} \end{Bmatrix} + \frac{\xi_{ql2} + \xi_{ql1}}{2}, \boldsymbol{w}_q = \frac{\xi_{ql2} - \xi_{ql1}}{2} \frac{\eta_{ql2} - \eta_{ql1}}{2} \begin{Bmatrix} 1.0 \\ 1.0 \end{Bmatrix}, \\ \boldsymbol{\eta}_q &= \frac{\eta_{ql2} - \eta_{ql1}}{2} \begin{Bmatrix} +1/\sqrt{3} \\ -1/\sqrt{3} \end{Bmatrix} + \frac{\eta_{ql2} + \eta_{ql1}}{2}, \end{aligned} \tag{35}$$

while $\xi_{ql1}, \xi_{ql2}, \eta_{ql1}, \eta_{ql2}$ are the limits as illustrated in Fig. 1**(c)**. One can calculate the numerical integration of *I-integral* (and/or *J-integral*) in a similar manner:

$$I^{(a,r)} = \sum_{s \in \mathcal{N}^I} \left(\sum_{q=1}^{n_{\text{sub}}} \sum_{p=1}^{2} \sum_{r=1}^{2} F_s \left(\xi_{q_p}, \eta_{q_r}\right) \left|\mathbf{J}^{\text{GL}}\right| \left|\mathbf{J}_s^{\text{NG}}\right| w_{q_p} w_{q_r} \right). \tag{36}$$

2.2 Classical continuum mechanics-peridynamics (CCM-PD) coupling strategy

The proposed coupling method builds upon the concept outlined in Galvanetto et al. (2016), where a coupled stiffness matrix is introduced and applied to address linear static problems in bond-based PD models. This approach is later expanded to address dynamic problems in Zaccariotto et al. (2018). Furthermore, an additional extension of this coupling method is discussed in Ni et al. (2021), specifically applied to state-based PD models.

To better elucidate the key characteristics of the proposed CCM–PD coupling strategy, a brief overview of the PD theory is necessary. For a more in-depth understanding, readers can refer to Silling (2000) for the bond-based PD theory, to Silling et al. (2007) for a comprehensive introduction to the more general state-based PD theory, and to Ongaro et al. (2021) for a

thorough analysis of the overall static equilibrium issues affecting CCM-PD coupled systems.

2.2.1 Overview of bond-based peridynamics

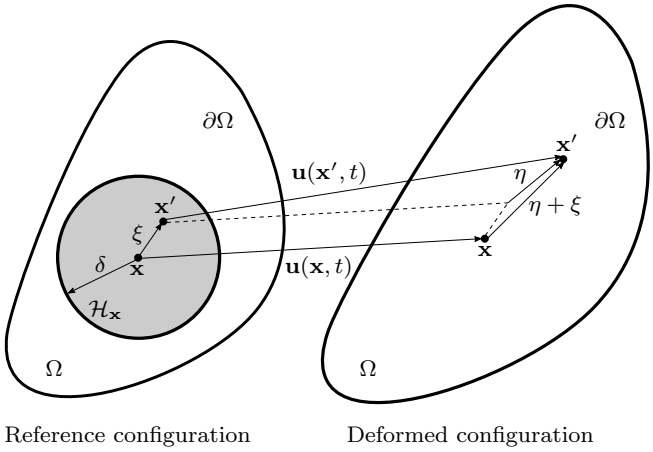

Fig. 3: Schematic representation of a generic PD domain Ω before and after deformation; the relative position vectors (initial and current) and the relative displacement vector between the material points $\mathbf{x}$ and $\mathbf{x}'$ are also depicted. Redrawn with modifications from Ongaro et al. (2023b).

In a spatial domain $\Omega \subset \mathbb{R}^p$, where p represents the spatial dimension, characterized by a PD model, each material point $\mathbf{x} \in \Omega$ interacts with all other material points situated within a finite neighborhood, $\mathcal{H}_\mathbf{x}$, of that specific material point (see Fig. 3). The equation of motion for any material point $\mathbf{x} \in \Omega$ at time $t \geqslant 0$, based on the bond-based PD formulation, is provided by Silling (2000):

$$\rho(\mathbf{x})\ddot{\mathbf{u}}(\mathbf{x}, t) = \int_{\mathcal{H}_\mathbf{x}} \mathbf{f}\left(\mathbf{u}(\mathbf{x}', t) - \mathbf{u}(\mathbf{x}, t), \mathbf{x}' - \mathbf{x}\right) \mathrm{d}V_{\mathbf{x}'} + \mathbf{b}(\mathbf{x}, t), \tag{37}$$

where ρ represents the mass density, $\ddot{\mathbf{u}}$ signifies the second time derivative of the displacement field $\mathbf{u}$, $\mathbf{f}$ denotes the pairwise force function, indicating the force per unit volume squared (or micro-force density) exerted by the material point $\mathbf{x}'$ on the material point $\mathbf{x}$, and $\mathbf{b}$ stands for a prescribed body force density field. The neighborhood $\mathcal{H}_\mathbf{x}$ is defined by:

$$\mathcal{H}_\mathbf{x} := \{\mathbf{x}' \in \Omega : \|\mathbf{x}' - \mathbf{x}\| \leq \delta\}, \tag{38}$$

where $\delta > 0$ represents the horizon. For material points within the body's bulk, specifically material points $\mathbf{x} \in \Omega$ located more than δ away from the body's boundary, $\partial\Omega$, the neighborhood $\mathcal{H}_{\mathbf{x}}$ is the integration region taken to be a line segment in one dimension, a disc in two dimensions, and a ball in three dimensions, all centered at $\mathbf{x}$. As depicted in Fig. 3, the representation of the initial relative position vector or the relative position vector of the two material points $\mathbf{x}$ and $\mathbf{x}'$ in the reference configuration is indicated by:

$$\boldsymbol{\xi} := \mathbf{x}' - \mathbf{x}, \tag{39}$$

which, in turn, indicates the standard PD notation for a bond. In the deformed configuration, at time $t > 0$, the displacement of the two material points $\mathbf{x}$ and $\mathbf{x}'$ would be $\mathbf{u}(\mathbf{x}, t)$ and $\mathbf{u}(\mathbf{x}', t)$, respectively. The relative displacement vector corresponding to this is defined by the following relation (see Fig. 3):

$$\boldsymbol{\eta} := \mathbf{u}(\mathbf{x}', t) - \mathbf{u}(\mathbf{x}, t). \tag{40}$$

The relative position vector of the two material points in the deformed configuration (or current relative position vector) is then denoted as $(\boldsymbol{\eta}+\boldsymbol{\xi})$. The force vector $\mathbf{f}$ (i.e., bond force), which contains all the constitutive information of the material, acts in the direction of $(\boldsymbol{\eta} + \boldsymbol{\xi})$. The general form of the pairwise force function $\mathbf{f}$ can be written as:

$$\mathbf{f}(\boldsymbol{\eta}, \boldsymbol{\xi}) = f(\boldsymbol{\eta}, \boldsymbol{\xi}) \frac{\boldsymbol{\eta} + \boldsymbol{\xi}}{\|\boldsymbol{\eta} + \boldsymbol{\xi}\|}. \tag{41}$$

Here, $f(\boldsymbol{\eta}, \boldsymbol{\xi})$ represents a scalar-valued even function defined according to the material type. For the prototype microelastic brittle (PMB) material model introduced in Silling and Askari (2005), $f(\boldsymbol{\eta}, \boldsymbol{\xi})$ is obtained from a differentiable scalar-valued function w, known as the pairwise potential function, in a manner that:

$$f(\boldsymbol{\eta}, \boldsymbol{\xi}) = \frac{\partial w(\boldsymbol{\eta}, \boldsymbol{\xi})}{\partial \boldsymbol{\eta}}, \tag{42}$$

where the function w is expressed by the following relation:

$$w(\boldsymbol{\eta}, \boldsymbol{\xi}) = \frac{cs^2 \|\boldsymbol{\xi}\|}{2}. \tag{43}$$

In this expression, c is known as the micromodulus constant, signifying the elastic stiffness of the bond, while s stands for the bond stretch and is formulated as:

$$s = \frac{\|\boldsymbol{\eta} + \boldsymbol{\xi}\| - \|\boldsymbol{\xi}\|}{\|\boldsymbol{\xi}\|}. \tag{44}$$

For the PMB material model (Silling and Askari, 2005), (42) is therefore given by:

$$f(\boldsymbol{\eta}, \boldsymbol{\xi}) = cs. \tag{45}$$

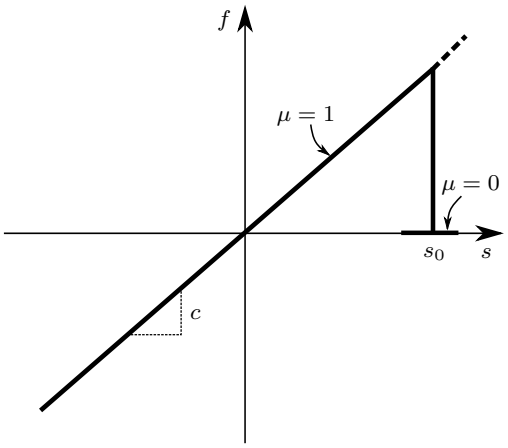

Fig. 4: Scalar bond force versus bond stretch for the PMB material model. Redrawn, with modifications, from Silling and Askari (2005).

For small deformations, considering (45) and assuming $\|\boldsymbol{\eta}\| \ll \delta$, the linearized form of (41) can be expressed as:

$$\mathbf{f}(\boldsymbol{\eta}, \boldsymbol{\xi}) = c\frac{\boldsymbol{\xi} \otimes \boldsymbol{\xi}}{\|\boldsymbol{\xi}\|^3}\boldsymbol{\eta}. \tag{46}$$

As thoroughly discussed in Silling and Askari (2005); Gerstle et al. (2005); Bobaru et al. (2009); Ha and Bobaru (2010), the micromodulus constant c can be linked to measurable macroscopic parameters, such as the Young's modulus E and the Poisson's ratio ν of the material. It's essential to emphasize that, due to the bond-based PD formulation relying on pairwise interactions, the Poisson's ratio is confined to a specific value depending on the scenario, namely, two-dimensional (plane stress or plane strain conditions) or three-dimensional case. Specifically, for three-dimensional and two-dimensional plane strain cases, the Poisson's ratio is fixed at $\nu = 1/4$, while for the two-dimensional plane stress case, it is constrained to $\nu = 1/3$ (Silling, 2000; Gerstle et al., 2005). Notably, this limitation has been overcome in the state-based version of the theory presented in Silling et al. (2007). The micromodulus constant, calculated using the correction factor γ introduced in Ongaro et al. (2021), which is utilized for the two-dimensional plane strain models considered in the present study can be computed as follows (Gerstle et al., 2005):

$$c = \frac{48E}{5\pi h\delta^3}\gamma, \tag{47}$$

where h indicates the plate thickness. In the PMB model, failure is introduced by setting a predetermined limit for the bond stretch s_0, commonly known as the critical stretch. A bond is considered broken when its current stretch sur-

passes this limit value, which can be correlated with measurable macroscopic quantities like the critical energy release rate of the material G_0 (Silling and Askari, 2005). For the two-dimensional plane strain models considered in the present work, the critical stretch can be computed as follows:

$$s_0 = \sqrt{\frac{5\pi G_0}{12E\delta}}. \tag{48}$$

In the case of mode I crack opening displacement, G_0 can be expressed as a function of the fracture toughness K_{Ic}, which is also a material property, by (Griffith, 1921; Irwin, 1957):

$$G_0 = \frac{K_{Ic}^2}{E'}, \tag{49}$$

where E' assumes either of the following two values:

$$E' = \begin{cases} E, & \text{plane stress condition,} \\ \\ \frac{E}{1-\nu^2}, & \text{plane strain condition.} \end{cases} \tag{50}$$

The breaking of a bond is an irreversible process, meaning that once a bond fails, the interaction between the two material points at its ends cannot be restored. Consequently, no tensile force can be sustained by the bond (see Fig. 4), and the contribution of this bond is no longer considered in the computation. In the PMB material model, the previously defined pairwise force function $\mathbf{f}(\boldsymbol{\eta}, \boldsymbol{\xi})$ (*cf.* (41)) can be rewritten as follows (Silling, 2000):

$$\mathbf{f}(\boldsymbol{\eta}, \boldsymbol{\xi}) = \mu(\boldsymbol{\xi}, t) cs \frac{\boldsymbol{\eta} + \boldsymbol{\xi}}{\|\boldsymbol{\eta} + \boldsymbol{\xi}\|}, \tag{51}$$

where $\mu(\boldsymbol{\xi}, t)$ is a scalar-valued function which introduces the history-dependence of the PMB material constitutive model and is therefore exploited as a bond-breaking parameter as follows (see Fig. 4):

$$\mu(\boldsymbol{\xi}, t) = \begin{cases} 1 \text{ if } & s(t') < s_0, \ 0 < t' < t, \\ \\ 0 & \text{otherwise.} \end{cases} \tag{52}$$

To conclude, the damage level at a material point $\mathbf{x}$ at time t is quantified through a local damage index, $\varphi(\mathbf{x}, t)$, which is defined as (Silling and Askari, 2005):

$$\varphi(\mathbf{x}, t) := 1 - \frac{\int_{\mathcal{H}_\mathbf{x}} \mu(\boldsymbol{\xi}, t) \mathrm{d}V_{\mathbf{x}'}}{\int_{\mathcal{H}_\mathbf{x}} \mathrm{d}V_{\mathbf{x}'}}. \tag{53}$$

The damage index is determined by the ratio of broken bonds to the total number of bonds initially linked to the material point $\mathbf{x}$. This index ranges

between 0 and 1, where $\varphi(\mathbf{x}, t) = 0$ signifies the undamaged state of the material, while $\varphi(\mathbf{x}, t) = 1$ indicates the complete disconnection of material point $\mathbf{x}$ from all neighboring material points (Silling and Askari, 2005).

Adopting the meshfree standard scheme introduced in Silling and Askari (2005), the discretized version of (37) can be written as follows:

$$\rho_i \ddot{\mathbf{u}}_i^n = \sum_j \mathbf{f}(\mathbf{u}_j^n - \mathbf{u}_i^n, \mathbf{x}_j - \mathbf{x}_i)\beta(\boldsymbol{\xi})V_j + \mathbf{b}_i^n \quad \forall \mathbf{x}_j \in \mathcal{H}_{\mathbf{x}_i}, \tag{54}$$

where the integral in (37) is replaced by a finite sum taken over all nodes j, referred to as family nodes, such that $\|\mathbf{x}_j - \mathbf{x}_i\| \leq \delta$, $\mathbf{f}$ is the pairwise force function that the family node j exerts on the source node i, n represents the time step number, subscripts refer to the node number, e.g., $\mathbf{u}_i^n = \mathbf{u}(\mathbf{x}_i, t^n)$, V_j is the discretized volume associated to the family node j, and $\beta(\boldsymbol{\xi})$ is a partial-volume correction factor used to evaluate the portion of V_j that falls within the neighborhood of the source node i, $\mathcal{H}_{\mathbf{x}_i}$, as recommended in Seleson (2014); Seleson and Littlewood (2016). The use of this correction factor is a consequence of the fact that the volumes associated to family nodes located close to the boundary of the neighborhood of i have only a partial overlapping with $\mathcal{H}_{\mathbf{x}_i}$. The introduction of this factor helps to improve the accuracy of the spatial integration, which is performed by adopting the one-point Gauss quadrature rule. In this study, we adopt the assumption of small strains and displacements, allowing us to express the linearized version of (54) in accordance with Silling and Askari (2005):

$$\rho_i \ddot{\mathbf{u}}_i^n = \sum_j \mathbf{C}(\mathbf{x}_j - \mathbf{x}_i)(\mathbf{u}_j^n - \mathbf{u}_i^n)\beta(\boldsymbol{\xi})V_j + \mathbf{b}_i^n \quad \forall \mathbf{x}_j \in \mathcal{H}_{\mathbf{x}_i}, \tag{55}$$

where $\mathbf{C}$ is the material's micromodulus function, a second-order tensor of the force vector $\mathbf{f}$ which is defined by the following relation (Silling, 2000):

$$\mathbf{C}(\boldsymbol{\xi}) := \frac{\partial \mathbf{f}}{\partial \boldsymbol{\eta}}(\mathbf{0}, \boldsymbol{\xi}) = \begin{bmatrix} \frac{\partial f_1}{\partial \eta_1}(\mathbf{0}, \boldsymbol{\xi}) & \frac{\partial f_1}{\partial \eta_2}(\mathbf{0}, \boldsymbol{\xi}) & \frac{\partial f_1}{\partial \eta_3}(\mathbf{0}, \boldsymbol{\xi}) \\ \frac{\partial f_2}{\partial \eta_1}(\mathbf{0}, \boldsymbol{\xi}) & \frac{\partial f_2}{\partial \eta_2}(\mathbf{0}, \boldsymbol{\xi}) & \frac{\partial f_2}{\partial \eta_3}(\mathbf{0}, \boldsymbol{\xi}) \\ \frac{\partial f_3}{\partial \eta_1}(\mathbf{0}, \boldsymbol{\xi}) & \frac{\partial f_3}{\partial \eta_2}(\mathbf{0}, \boldsymbol{\xi}) & \frac{\partial f_3}{\partial \eta_3}(\mathbf{0}, \boldsymbol{\xi}) \end{bmatrix}. \tag{56}$$

In this study, the spatial integration of the model domain is performed by implementing the standard meshfree scheme (Silling and Askari, 2005) and considering a uniform distribution of nodes, where the distance between two nearest neighboring nodes is referred to as grid spacing. We employ a uniform grid with $\Delta x = \Delta y$, where Δx and Δy are the grid spacings in the x- and y-directions, respectively. The discretized representation of the PD horizon δ

is described by the following relationship:

$$\delta = m\Delta x, \tag{57}$$

where m represents the ratio of the PD horizon δ to the grid spacing Δx and is commonly known as the m-ratio. The specific value of the m-ratio is associated with the count of family nodes situated within the neighborhood $\mathcal{H}_{\mathbf{x}_i}$ of a source node i. Hence, the PD horizon δ and the m-ratio are the two parameters influencing the number of interactions to be accounted for in each node within a discretized PD model.

2.2.2 CCM-PD coupling approach for brittle fracture modeling

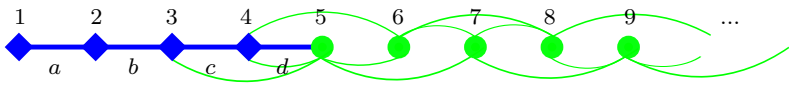

Fig. 5: Representation of the CCM-PD coupled model in a one-dimensional system. FEM nodes are denoted by blue diamonds, PD nodes by green circles, FEM elements by blue thick straight lines, and PD bonds by green thin curved lines. Adapted from Galvanetto et al. (2016).

In the CCM-PD coupling strategy proposed in Galvanetto et al. (2016); Zaccariotto et al. (2018), the domain Ω is described partially using a CCM model discretized with the FEM, while the remaining part utilizes a PD model discretized with a meshfree standard scheme based on Silling and Askari (2005). Effective coupling between the two regions is essential for ensuring proper force transfer. Fig. 5 illustrates the CCM-PD coupled model in a one-dimensional system, with diamonds representing FEM nodes, circles representing PD nodes, thick straight lines indicating FEM elements, and curved thin lines representing PD bonds.

Nodes are categorized as FEM or PD types, ensuring no overlapping region in terms of node nature. In the provided example (see Fig. 5), the horizon δ is twice the grid spacing (i.e., $\delta = 2\Delta x$). Each PD node is connected by PD bonds to four other nodes, such as nodes 5, 6, 8, and 9 interacting with node 7, referred to as its family nodes. FEM nodes connect through FEM elements, while PD nodes connect through PD bonds.

At the CCM-PD transition, the last FEM node (node 4 in Fig. 5) is assumed to connect to the PD region through a single FEM element (element d in Fig. 5). Simultaneously, the first PD node (node 5 in Fig. 5) is nonlocally connected by PD bonds to all nodes, whether FEM or PD nodes, within its neighborhood. All PD nodes with neighborhoods containing FEM nodes nonlocally interact through PD bonds with those FEM nodes.

The proposed CCM-PD coupling technique operates under the assumption that internal forces acting on a node correspond to the nature of that node. Specifically, FEM nodes experience internal forces computed using the FEM approach, while PD nodes exclusively encounter internal forces determined through the PD formulation. A designated coupling zone facilitates force exchange between the CCM and PD sections of the domain.

In the illustrated example, the coupling zone comprises FEM nodes 3 and 4, PD nodes 5 and 6, PD bonds $3-5$, $4-5$, and $4-6$, along with FEM element d. The coupling method ensures that the internal force exerted by FEM element d exclusively affects FEM node 4. Similarly, the internal forces from PD bonds $3-5$ and $4-5$, as well as $4-6$, exclusively impact PD nodes 5 and 6, respectively. This approach guarantees that the assembly of the global stiffness matrix maintains equilibrium equations for FEM nodes with terms solely from the FEM approach, while equilibrium equations for PD nodes include terms derived exclusively from the PD formulation.

The case of Fig. 5 leads to the formulation of the following system of equations (see Ongaro et al. (2021)):

$$\begin{bmatrix} l & -l & 0 & 0 & 0 & 0 & 0 & 0 & 0 & \vdots \\ -l & 2l & -l & 0 & 0 & 0 & 0 & 0 & 0 & \vdots \\ 0 & -l & 2l & -l & 0 & 0 & 0 & 0 & 0 & \vdots \\ 0 & 0 & -l & 2l & -l & 0 & 0 & 0 & 0 & \vdots \\ 0 & 0 & -\frac{1}{4}p & -p & \frac{5}{2}p & -p & -\frac{1}{4}p & 0 & 0 & \vdots \\ 0 & 0 & 0 & -\frac{1}{4}p & -p & \frac{5}{2}p & -p & -\frac{1}{4}p & 0 & \vdots \\ 0 & 0 & 0 & 0 & -\frac{1}{4}p & -p & \frac{5}{2}p & -p & -\frac{1}{4}p & \vdots \\ 0 & 0 & 0 & 0 & \cdots & \cdots & \cdots & \ddots & \vdots & \vdots \\ \cdots & \cdots & \cdots & \cdots & \cdots & \cdots & \cdots & \cdots & \ddots & \vdots \end{bmatrix} \begin{bmatrix} u_1 \\ u_2 \\ u_3 \\ u_4 \\ u_5 \\ \vdots \\ \vdots \\ \vdots \\ u_N \end{bmatrix} = \begin{bmatrix} F_1 \\ F_2 \\ F_3 \\ F_4 \\ F_5 \\ \vdots \\ \vdots \\ \vdots \\ F_N \end{bmatrix}, \tag{58}$$

where l is defined as $EA/\Delta x$ (Zienkiewicz and Taylor, 2005), p is $cA^2\Delta x$ (Bobaru et al., 2009), N represents the total number of nodes (including FEM and PD nodes), $\{u_i\}_{i=1,\dots,N}$ denotes the nodal displacements, $\{F_i\}_{i=1,\dots,N}$ signifies the external nodal forces, E is Young's modulus, c is the micromodulus constant, and the cross-sectional area A is assumed to be $A = 1$. The meshfree PD discretization in (58) utilizes a partial-volume correction (Seleson and Littlewood, 2016), applying a factor of $\frac{1}{2}$ to the contribution of second-nearest neighbors. While the solution of a single equation ensures node equilibrium, achieving overall equilibrium for the entire structure requires that the sum of external nodal forces equals zero. The interested reader may refer to Ongaro et al. (2021) for an in-depth analysis of the overall equilibrium issues which affect the proposed approach even if it precisely meets

the criteria of standard numerical tests for static coupling problems, including scenarios with imposed rigid body motions and uniform or linear strain distributions (Galvanetto et al., 2016; Zaccariotto et al., 2018).

3 Numerical Simulation

In this section, the results obtained from LEFM based XFEM and CCM-PD coupled models are compared for the benchmark problem of uniaxially deformed finite plate with an edge crack, promoting self-similar (Mode I) crack growth.

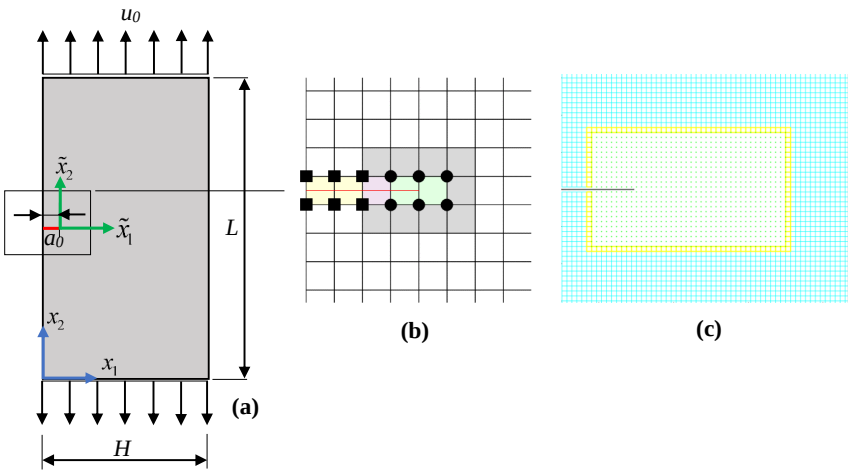

Fig. 6: **(a)** Schematic of the case study and corresponding discretization at the vicinity of the crack tip for **(b)** XFEM, **(c)** CCM-PD models. In the CCM-PD model, green circles are PD nodes, light blue (empty) squares are FEM elements, whereas yellow (empty) squares represents hybrid FEM elements, i.e., FEM elements characterized by at least one PD node within its 4 constitutive nodes.

The dimensions of the model are arranged as;

$$H = 11\,(\text{mm}),\ L = 21\,(\text{mm}),\ a_0 = 0.1H, \tag{59}$$

where L, H, and a_0 refer to height, width, and initial crack length, respectively, as illustrated in Fig. 6(**a**) while the analyses are performed for following material parameters;

$$E = 10 \text{ (MPa)}, \quad \nu = 0.25, \quad G_0 = 0.367 \text{ (MPa mm)}, \tag{60}$$

with G_0 being the fracture energy that is responsible for bond breaking in PD approach and crack propagation in LEFM. The upper and lower edges of the plate are subjected to a uniform and opposite prescribed displacement field of u_0;

$$u_2(x_1, L) = -u_2(x_1, 0) = u_0 = 0.01(\text{mm}). \tag{61}$$

For XFEM model, the domain is uniformly discretized into 44×83 quadrilateral elements. The enriched elements are sub-divided into 4×4 quads with each one having 2×2 Gauss-sampling points for numerical integration. Here the number of elements along horizontal and vertical directions are selected in such a way to ensure that the crack passes through the middle of the elements and crack tip lies at the edge of the element, as illustrated in Fig. 6(**b**). For CCM-PD approach, on the other hand, the model is discretized by considering an internal PD region as schematically shown in Fig. 6(**c**). The PD portion of the domain is a rectangle of edge lengths $L_{PDx} = 2.73$ (mm) and $L_{PDy} = 1.67$ (mm), and its centre has coordinates $(1.70, 10.5)$ (mm). The remaining part of the domain, the CCM region, is discretized using four-node square plane strain FEM elements. The stiffness matrix for these elements is computed using exact integration (Zienkiewicz and Taylor, 2005). The domain is discretized using a uniform grid with $\Delta x = \Delta y = 0.067$ (mm). We assume a CCM model given by the classical linear elasticity plane strain isotropic model and a PD model given by a linear bond-based isotropic model. The PD horizon is taken as $\delta = 0.267$ (mm) (i.e., $m = 4$) and the micromodulus constant c has been evaluated through (47) by considering a value of the correction factor γ equal to 0.988895997195466 (see Ongaro et al. (2021) for details on γ computation). The PD portion of the domain employs a meshfree discretization with a partial-volume correction (Seleson, 2014).

For coupled CCM-PD model, the quasi-static fracture analysis is performed by exploiting the sequentially linear analysis (SLA) procedure, as accurately discussed in Ni et al. (2019). This involves assembling the coupled stiffness matrix and subsequently applying boundary conditions. Given the linear-brittle constitutive behavior of the PD bonds in this study, a structure subjected to an increasing load (either applied force or displacement) exhibits linear behavior until the first bond breaks. The PD portion of the coupled stiffness matrix must then be adjusted by removing the contribution of the broken bond. Subsequently, the structure, with slightly reduced stiffness, resumes linear behavior until the next PD bond breakage. Using the SLA procedure (Ongaro et al., 2022), the structural problem is solved to obtain the vertical nodal reaction forces of the system, which are then exploited to compute the resulting uniaxial stresses at the upper and lower edges of the plate, similar to XFEM model.

As the first step, the resulting stress intensity factor (SIF) (K_I) is compared with the analytical one given in the literature for the validation of the XFEM in-house code. According to Tada et al. (2000), the SIF can be

calculated using following formulation for the considered case study:

$$K_I = \mathrm{SF}\,(a_0/H)\,\sigma_0\sqrt{\pi a_0}. \tag{62}$$

Here SF is an empirical formulation that is used to account for the scale factor related to the geometry, which takes the value of 1.17 for the considered ratio between a_0 and H, while σ_0 is the uniform uniaxial stress applied at the top and bottom edges. As in our case, the model is deformed through a prescribed displacement rather than load, the stress that is emerged at the edges should be calculated as a post-processing data, which turns out to be 9.993 MPa for XFEM model. Accordingly, the analytical value of SIF is:

$$K_I^{\mathrm{Analytical}} = 20.79\mathrm{MPa}\sqrt{\mathrm{mm}}. \tag{63}$$

Meanwhile the SIF that is detected from the XFEM model using the domain form of I-integral with a radius of $r_I = 2.5l_x$ is as follows:

$$K_I^{\mathrm{XFEM}} = 19.85\mathrm{MPa}\sqrt{\mathrm{mm}}. \tag{64}$$

As one can see, the error between analytical and numerical SIF is about 4.75%, while this variation can be attributed to the non-uniform stress field along the edges. In fact, if the prescribed displacements are replaced with a stress of $\sigma_0 = 9.993$ MPa and the simulation is re-run for XFEM model, one can obtain the resulting SIF as $20.71\mathrm{MPa}\sqrt{\mathrm{mm}}$, for which the difference is less than 0.4%.

So far the accuracy of the XFEM model is justified, now the consistency between the outputs of LEFM based XFEM and CCM-PD methodologies should be checked. For this purpose, the crack mouth opening displacements (CMOD) and resulting uniaxial stresses are compared for the initial state before crack starts to propagate. It can be seen that, there is a very good agreement between results of CCM-PD and LEFM/XFEM as CMOD and σ_{22} values are attained as; $0.005374 - 0.005317$ (mm), and $9.992 - 9.993$ (MPa), respectively.

Finally, as the scope of this study, the variation of fracture parameters (CMOD, σ_{22}) with crack evaluation are investigated for both approaches to check the possibility of having a one to one correspondence between LEFM and bond-based PD models. In doing so, the outputs obtained from LEFM based XFEM and coupled CCM-PD are plotted on the same graph as illustrated in Fig. 7. As one can see, a perfect agreement is attained between the two methodologies that are based on different principles; although in both, the domain is treated as a continuum, LEFM exploits the advantages of field descriptions while PD accounts for interaction in-between each material point within a finite distance. Accordingly, in latter, the crack and its propagation can be modeled inherently as a material response that depends on the failure of interactions between material points constituting the continuum, whereas in the former, a pre-defined fracture criterion is required to detect the direc-

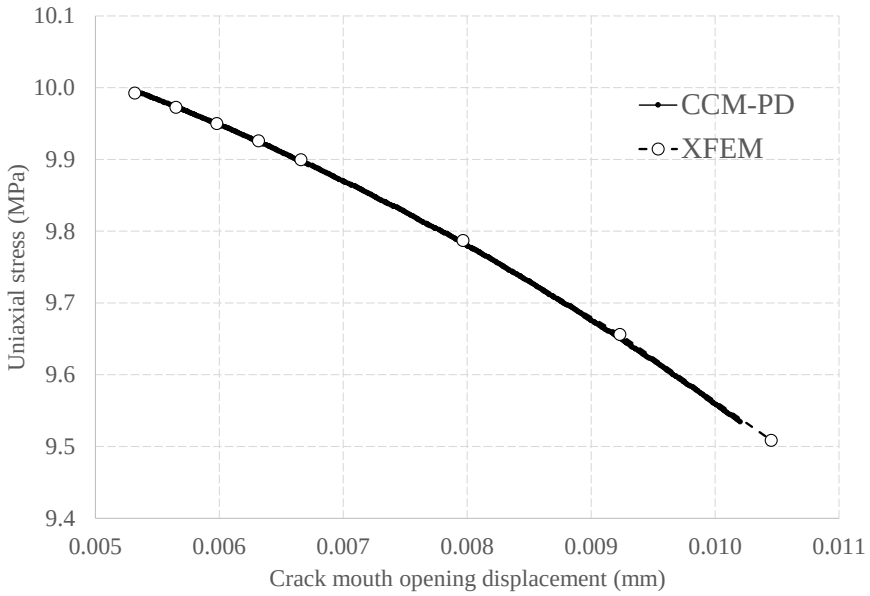

Fig. 7: Variation of crack mouth opening displacement (CMOD) vs uniaxial stress during crack propagation plotted for XFEM and CCM-PD models.

tion of propagation. Nevertheless, as in the present study, the domain with a straight crack is under uniaxial tension, all of the fracture criteria will provide same output; self similar crack growth (i.e., Mode I). This straight crack trajectory is also evident from Fig. 8 that shows the damage map (*cf.* (53)) for CCM-PD model (Fig. 8(**a**)) and two steps of crack evaluation for XFEM model (Fig. 8(**b**)), respectively.

As the consistency between the CCM-PD and XFEM models is verified, one should examine their efficiency in terms of computational cost by comparing the simulation run times which are 1999.71 and 1919.62 seconds, and performed on two different computers; Intel(R) Core(TM) i7-8750H CPU @ 2.20GHz 2.21 GHz processor with 16 GB RAM and Intel(R) Core(TM) i5-8250U CPU @ 1.60GHz 1.80 GHz processor with 8 GB RAM, respectively. Although the computational expense is almost the same, one should acknowledge the simple nature of the case study under consideration, as for mixed mode case accurate detection of the direction of crack propagation might require a more refined analysis procedure.

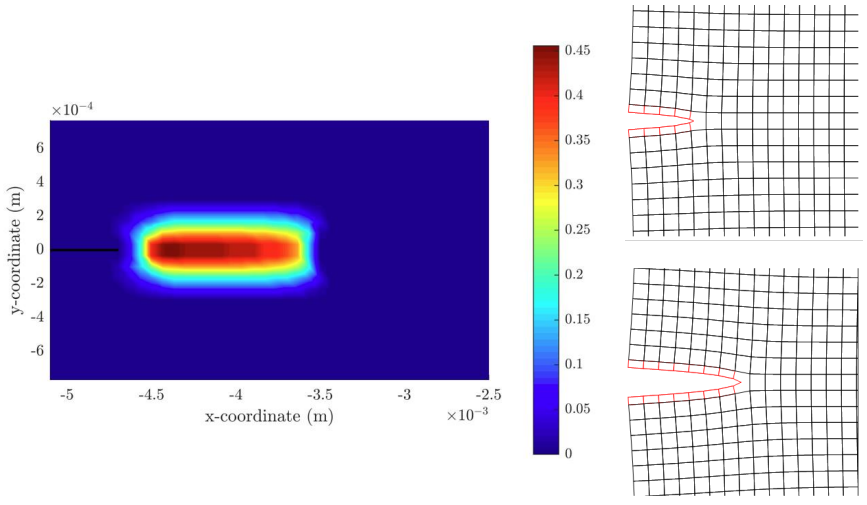

Fig. 8: Crack trajectory of models **(a)** CCM-PD model: Damage map derived after performing 500 steps of the SLA procedure (To enhance clarity, only the PD portion of the domain is depicted in the figure), **(b)** XFEM model: Zoom-in looks of two steps during propagation (The deformation is exaggerated 50 times for visual purposes).

4 Conclusions

Accurately modeling material response possesses a significant challenge in characterizing the crack propagation phenomenon for which various analytical and numerical methods have been employed. Among those the linear elastic fracture mechanics (LEFM) and bond-based peridynamics (PD) are employed in this study following their popularity in the field of fracture mechanics.

Both approaches treat the domain as continuum, yet LEFM exploits the advantages of field description, whereas PD explicitly accounts for the interactions between each material point located within a finite neighborhood. Accordingly, in LEFM, the real crack topology is modeled as a discontinuity and the crack path is tracked based on the implemented fracture criterion without following actual interactions between particles. On the other hand, in PD, crack nucleation and propagation are represented by the irreversible breaking of the bonds connecting different material points, through which the evaluation of the crack path is traced directly without having to define any ad hoc criteria. The corresponding numerical analyses are performed through

LEFM based XFEM model and a CCM-PD coupling approach, respectively, for computational ease.

For comparison, an uniformly deformed finite rectangular plate with a straight edge crack, promoting self similar crack growth (i.e. Mode I), is examined exploiting both approaches. The results reveal the promising nature of correspondence between those methodologies, as a perfect agreement is achieved regarding crack mouth opening displacements and resulting uniaxial stresses. For the considered benchmark problem, no significant difference in terms of computational time is encountered, yet it should be kept in mind that a more comprehensive examination should be made including shearing and mixed mode cases.

This output motivates the Authors to extend the work to the structures represented within non-classical theories such as micropolar model (Tuna and Trovalusci, 2020; Tuna et al., 2020) in which the material particles is assumed to be interacted not only by forces but also by couple of forces, requiring a more enhanced PD model.

Acknowledgements This work is supported by MIUR under the research project PNRR - CN1- Spoke6 - B83C22002940006. The Authors also acknowledge the support of PRIN 2020, Project 2020F23HZ7003 (J35F22000640001).

References

Aksoylu, B. and Parks, M. L. (2011). Variational theory and domain decomposition for nonlocal problems. *Applied Mathematics and Computation*, 217(14):6498–6515.

Askari, E., Bobaru, F., Lehoucq, R., Parks, M., Silling, S., and Weckner, O. (2008). Peridynamics for multiscale materials modeling. In *Journal of Physics: Conference Series*, volume 125, page 012078. IOP Publishing.

Ayatollahi, M., Rashidi Moghaddam, M., and Berto, F. (2015). A generalized strain energy density criterion for mixed mode fracture analysis in brittle and quasi-brittle materials. *Theoretical and Applied Fracture Mechanics*, 79:70–76.

Barenblatt, G. (1962). The mathematical theory of equilibrium cracks in brittle fracture. volume 7 of *Advances in Applied Mechanics*, pages 55–129. Elsevier.

Belytschko, T. and Black, T. (1999). Elastic crack growth in finite elements with minimal remeshing. *International Journal for Numerical Methods in Engineering*, 45:601–620.

Bobaru, F., Foster, J. T., Geubelle, P. H., and Silling, S. A. (2016). *Handbook of peridynamic modeling*. CRC press.

Bobaru, F. and Hu, W. (2012). The meaning, selection, and use of the peridynamic horizon and its relation to crack branching in brittle materials. *International journal of fracture*, 176:215–222.

Bobaru, F., Yang, M., Alves, L. F., Silling, S. A., Askari, E., and Xu, J. (2009). Convergence, adaptive refinement, and scaling in 1d peridynamics. *International Journal for Numerical Methods in Engineering*, 77(6):852–877.

Bourdin, B., Francfort, G., and Marigo, J.-J. (2008). The variational approach to fracture. *Journal of Elasticity*, 91:1573–2681.

Chen, B., Yu, T., Natarajan, S., Zhang, Q., and Bui, T. Q. (2022). Three-dimensional dynamic and quasi-static crack growth by a hybrid xfem-peridynamics approach. *Engineering Fracture Mechanics*, 261:108205.

Chen, F. and Shield, R. (1977). Conservation laws in elasticity of the j-integral type. *Journal of Applied Mathematics and Physics*, 28:1–22.

Cherepanov, G. P. (1967). The Propagation of Cracks in a Continuous Medium. *Journal of Applied Mathematics and Mechanic*, 31:503–512.

Chiaia, B., Vervuurt, A., and Van Mier, J. (1997). Lattice model evaluation of progressive failure in disordered particle composites. *Engineering Fracture Mechanics*, 57:301–318.

Cundall, P. A. and Strack, O. D. L. (1979). A discrete numerical model for granular assemblies. *Géotechnique*, 29(1):47–65.

Daux, C., Moes, N., Dolbow, J., Sukumar, N., and Belytschko, T. (2000). Arbitrary cracks and holes with the extended finite element method. *International Journal for Numerical Methods in Engineering*, 48:1741–1760.

de Borst, R., Benallal, A., and Heeres, O. (1996). A gradient-enhanced damage approach to fracture. *Journal de Physique IV Proceedings*, 06:491–502.

Dolbow, J. (1999). *An Extended Finite Element Method with Discontinuous Enrichment for Applied Mechanics*. PhD thesis, Northwestern University.

Dugdale, D. (1960). Yielding of steel sheets containing slits. *Journal of the Mechanics and Physics of Solids*, 8:100–104.

D'Elia, M. and Bochev, P. (2021). Formulation, analysis and computation of an optimization-based local-to-nonlocal coupling method. *Results in Applied Mathematics*, 9:100129.

D'Elia, M. and Bochev, P. B. (2015). Optimization–based coupling of nonlocal and local diffusion models. *MRS Online Proceedings Library (OPL)*, 1753:mrsf14–1753.

D'Elia, M., Li, X., Seleson, P., Tian, X., and Yu, Y. (2021). A review of local-to-nonlocal coupling methods in nonlocal diffusion and nonlocal mechanics. *Journal of Peridynamics and Nonlocal Modeling*, pages 1–50.

Erdogan, F. and Sih, G. C. (1963). On the Crack Extension in Plates Under Plane Loading and Transverse Shear. *Journal of Basic Engineering*, 85:519–525.

Eshelby, J. (1974). The calculation of energy release rates. In Sih, G., editor, *Conference on Prospects of Advanced Fracture Mechanics*, Delft.

Fleming, M., Chu, Y., Moran, B., and T., B. (1997). Enriched element-free galerkin methods for crack tip fields. *International Journal for Numerical Methods in Engineering*, 40:1483–1504.

Francfort, G. and Marigo, J.-J. (1998). Revisiting brittle fracture as an energy minimization problem. *Journal of the Mechanics and Physics of Solids*, 46:1319–1342.

Galvanetto, U., Mudric, T., Shojaei, A., and Zaccariotto, M. (2016). An effective way to couple fem meshes and peridynamics grids for the solution of static equilibrium problems. *Mechanics Research Communications*, 76:41–47.

Gdoutos, E. (2006). *Fracture Mechanics: An Introduction*. Solid Mechanics and Its Applications. Springer Netherlands.

Gerstle, W., Sau, N., and Silling, S. (2005). Peridynamic modeling of plain and reinforced concrete structures.

Griffith, A. (1921). The phenomena of rupture and flow in solids. *Philosophical Transactions of the Royal Society of London Series A*, 221:163–198.

Ha, Y. D. and Bobaru, F. (2010). Studies of dynamic crack propagation and crack branching with peridynamics. *International Journal of Fracture*, 162:229–244.

Ha, Y. D. and Bobaru, F. (2011). Characteristics of dynamic brittle fracture captured with peridynamics. *Engineering Fracture Mechanics*, 78(6):1156–1168.

Han, F. and Lubineau, G. (2012). Coupling of nonlocal and local continuum models by the arlequin approach. *International Journal for Numerical Methods in Engineering*, 89(6):671–685.

Han, F., Lubineau, G., Azdoud, Y., and Askari, A. (2016). A morphing approach to couple state-based peridynamics with classical continuum mechanics. *Computer methods in applied mechanics and engineering*, 301:336–358.

Hermann, A., Shojaei, A., Steglich, D., Höche, D., Zeller-Plumhoff, B., and Cyron, C. J. (2022). Combining peridynamic and finite element simulations to capture the corrosion of degradable bone implants and to predict their residual strength. *International Journal of Mechanical Sciences*, 220:107143.

Hou, C., Jin, X., Fan, X., Xu, R., and Wang, Z. (2019). A generalized maximum energy release rate criterion for mixed mode fracture analysis of brittle and quasi-brittle materials. *Theoretical and Applied Fracture Mechanics*, 100:78–85.

Hu, W., Ha, Y. D., and Bobaru, F. (2012). Peridynamic model for dynamic fracture in unidirectional fiber-reinforced composites. *Computer Methods in Applied Mechanics and Engineering*, 217:247–261.

Huang, R., Sukumar, N., and Prevost, J. (2003). Modelling quasi-static crack growth with the extended finite element method part ii: Numerical applications. *International Journal of Solids and Structures*, 40:7539–7552.

Hussain, M., Pu, S., Underwood, J., International, A., (N.Y.), W. A., for Testing, A. S., and Materials (1973). *Strain Energy Release Rate for a Crack Under Combined Mode I and Mode II.* Defense Technical Information Center.

Inglis, C. (1913). Stresses in a plate due to the presence of cracks and sharp corners. volume 137, pages 3–17.

Irwin, G. (1968). Linear fracture mechanics, fracture transition, and fracture control. *Engineering Fracture Mechanics*, 1:241–257.

Irwin, G. R. (1948). Fracture Dynamics, Fracturing of Metals. *American Society for Metals*, pages 147–166.

Irwin, G. R. (1957). Analysis of Stresses and Strains Near the End of a Crack Traversing a Plate. *Journal of Applied Mechanics*, 24:361–364.

Jiang, F. and Shen, Y. (2022). A quasi-nonlocal coupling method for bond-based peridynamics with classical continuum mechanics. *Engineering Computations*, 39(2):554–573.

Laborde, P., Pommier, J., Renard, Y., and Salaün, M. (2005). High-order extended finite element method for cracked domains. *International Journal for Numerical Methods in Engineering*, 64:354–381.

Le, Q. and Bobaru, F. (2018). Surface corrections for peridynamic models in elasticity and fracture. *Computational Mechanics*, 61:499–518.

Lubineau, G., Azdoud, Y., Han, F., Rey, C., and Askari, A. (2012). A morphing strategy to couple non-local to local continuum mechanics. *Journal of the Mechanics and Physics of Solids*, 60(6):1088–1102.

Macek, R. W. and Silling, S. A. (2007). Peridynamics via finite element analysis. *Finite elements in analysis and design*, 43(15):1169–1178.

Mariano, P. M. and Trovalusci, P. (1999). Constitutive relations for elastic microcracked bodies: from a lattice model to a multifield continuum description. *International Journal of Damage Mechanics*, 8(2):153–173.

Miehe, C., Welschinger, F., and Hofacker, M. (2010). Thermodynamically consistent phase-field models of fracture: Variational principles and multi-field fe implementations. *International Journal for Numerical Methods in Engineering*, 83:1273–1311.

Moes, N., Dolbow, J., and Belytschko, T. (1999). A finite element method for crack growth without remeshing. *International Journal for Numerical Methods in Engineering*, 46:131–150.

Moran, B. and Shih, C. (1987). A general treatment of crack tip contour integrals. *International Journal of Fracture*, 35:295–310.

Moës, N., Stolz, C., Bernard, P.-E., and Chevaugeon, N. (2011). A level set based model for damage growth: The thick level set approach. *International Journal for Numerical Methods in Engineering*, 86:358–380.

Ni, T., Zaccariotto, M., Zhu, Q.-Z., and Galvanetto, U. (2019). Static solution of crack propagation problems in peridynamics. *Computer Methods in Applied Mechanics and Engineering*, 346:126–151.

Ni, T., Zaccariotto, M., Zhu, Q.-Z., and Galvanetto, U. (2021). Coupling of fem and ordinary state-based peridynamics for brittle failure analysis in 3d. *Mechanics of advanced materials and structures*, 28(9):875–890.

Nuismer, R. J. (1975). An energy release rate criterion for mixed mode fracture. *International Journal of Fracture*, 11:245–250.

Ongaro, G., Bertani, R., Galvanetto, U., Pontefisso, A., and Zaccariotto, M. (2022). A multiscale peridynamic framework for modelling mechanical properties of polymer-based nanocomposites. *Engineering Fracture Mechanics*, 274:108751.

Ongaro, G., Pontefisso, A., Zeni, E., Lanero, F., Famengo, A., Zorzi, F., Zaccariotto, M., Galvanetto, U., Fiorentin, P., Gobbo, R., et al. (2023a). Chemical and mechanical characterization of unprecedented transparent epoxy–nanomica composites—new model insights for mechanical properties. *Polymers*, 15(6):1456.

Ongaro, G., Seleson, P., Galvanetto, U., Ni, T., and Zaccariotto, M. (2021). Overall equilibrium in the coupling of peridynamics and classical continuum mechanics. *Computer Methods in Applied Mechanics and Engineering*, 381:113515.

Ongaro, G., Shojaei, A., Mossaiby, F., Hermann, A., Cyron, C. J., and Trovalusci, P. (2023b). Multi-adaptive spatial discretization of bond-based peridynamics. *International Journal of Fracture*, pages 1–24.

Orowan, E. (1949). Fracture and strength of solids. *Reports on Progress in Physics*, 12:185.

Ostoja-Starzewski, M. and Wang, G. (2006). Particle modeling of random crack patterns in epoxy plates. *Probabilistic Engineering Mechanics*, 21:267–275.

Peerlings, R., De Borst, R., Brekelmans, W., and De Vree, J. (1996). Gradient enhanced damage for quasi-brittle materials. *International Journal for Numerical Methods in Engineering*, 39(19):3391–3403.

Pijaudier-Cabot, G. and Bažant, Z. P. (1987). Nonlocal damage theory. *Journal of Engineering Mechanics*, 113:1512–1533.

Rice, J. R. (1968). A Path Independent Integral and the Approximate Analysis of Strain Concentration by Notches and Cracks. *Journal of Applied Mechanics*, 35:379–386.

Scabbia, F., Zaccariotto, M., and Galvanetto, U. (2021). A novel and effective way to impose boundary conditions and to mitigate the surface effect in state-based peridynamics. *International Journal for Numerical Methods in Engineering*, 122(20):5773–5811.

Scabbia, F., Zaccariotto, M., and Galvanetto, U. (2023). A new surface node method to accurately model the mechanical behavior of the boundary in 3d state-based peridynamics. *Journal of Peridynamics and Nonlocal Modeling*, pages 1–35.

Seleson, P. (2014). Improved one-point quadrature algorithms for two-dimensional peridynamic models based on analytical calculations. *Computer Methods in Applied Mechanics and Engineering*, 282:184–217.

Seleson, P., Beneddine, S., and Prudhomme, S. (2013a). A force-based coupling scheme for peridynamics and classical elasticity. *Computational Materials Science*, 66:34–49.

Seleson, P., Gunzburger, M., and Parks, M. L. (2013b). Interface problems in nonlocal diffusion and sharp transitions between local and nonlocal domains. *Computer Methods in Applied Mechanics and Engineering*, 266:185–204.

Seleson, P., Ha, Y. D., and Beneddine, S. (2015). Concurrent coupling of bond-based peridynamics and the navier equation of classical elasticity by blending. *International Journal for Multiscale Computational Engineering*, 13(2).

Seleson, P. and Littlewood, D. J. (2016). Convergence studies in meshfree peridynamic simulations. *Computers & Mathematics with Applications*, 71(11):2432–2448.

Sheikhbahaei, P., Mossaiby, F., and Shojaei, A. (2023). Analyzing cyclic loading behavior of concrete structures: A peridynamic approach with softening models and validation. *Theoretical and Applied Fracture Mechanics*, 128:104165.

Shojaei, A., Hermann, A., Seleson, P., and Cyron, C. J. (2020). Dirichlet absorbing boundary conditions for classical and peridynamic diffusion-type models. *Computational Mechanics*, 66:773–793.

Shojaei, A., Mudric, T., Zaccariotto, M., and Galvanetto, U. (2016). A coupled meshless finite point/peridynamic method for 2d dynamic fracture analysis. *International Journal of Mechanical Sciences*, 119:419–431.

Shojaei, A., Zaccariotto, M., and Galvanetto, U. (2017). Coupling of 2d discretized peridynamics with a meshless method based on classical elasticity using switching of nodal behaviour. *Engineering Computations*, 34(5):1334–1366.

Sih, G. C. (1974). Strain-energy-density factor applied to mixed mode crack problems. *International Journal of Fracture*, 10:305–321.

Silling, S., Littlewood, D., and Seleson, P. (2015). Variable horizon in a peridynamic medium. *Journal of Mechanics of Materials and Structures*, 10(5):591–612.

Silling, S. A. (2000). Reformulation of elasticity theory for discontinuities and long-range forces. *Journal of the Mechanics and Physics of Solids*, 48(1):175–209.

Silling, S. A. (2010). Linearized theory of peridynamic states. *Journal of Elasticity*, 99:85–111.

Silling, S. A. and Askari, E. (2005). A meshfree method based on the peridynamic model of solid mechanics. *Computers & structures*, 83(17-18):1526–1535.

Silling, S. A., Epton, M., Weckner, O., Xu, J., and Askari, E. (2007). Peridynamic states and constitutive modeling. *Journal of elasticity*, 88:151–184.

Smith, D., Ayatollahi, M., and Pavier, M. (2006). On the consequences of t-stress in elastic brittle fracture. *Proceedings of the Royal Society A*, 462:2415–2437.

Stern, M., Becker, E., and Dunham, R. (1976). A contour integral computation of mixed-mode stress intensity factors. *International Journal of Fracture*, 12:359–368.

Sukumar, N. and Prevost, J. (2003). Modelling quasi-static crack growth with the extended finite element method part i: Computer implementation. *International Journal of Solids and Structures*, 40:7513–7537.

Sun, C. and Jin, Z.-H. (2012). Chapter 3 - the elastic stress field around a crack tip. In Sun, C. and Jin, Z.-H., editors, *Fracture Mechanics*, pages 25–75. Academic Press, Boston.

Tada, H., Paris, P. C., and Irwin, G. R. (2000). *The Stress Analysis of Cracks Handbook*. ASMR Press.

Tadmor, E. and Miller, R. (2011). *Modeling Materials: Continuum, Atomistic and Multiscale Techniques*. Cambridge University Press.

Topin, V., Delenne, J., and Radjai, F. (2007). Strength and failure of cemented granular matter. *The European Physical Journal E*, 23:413–429.

Tuna, M., Leonetti, L., Trovalusci, P., and Kirca, M. (2020). 'explicit'and 'implicit'non-local continuous descriptions for a plate with circular inclusion in tension. *Meccanica*, 55:927–944.

Tuna, M. and Trovalusci, P. (2020). Scale dependent continuum approaches for discontinuous assemblies:'explicit'and 'implicit'non-local models. *Mechanics Research Communications*, 103:103461.

Yau, J., Wang, S., and Corten, H. (1980). A mixed-mode crack analysis of isotropic solids using conservation laws of elasticity. *Journal of Applied Mechanics, Transactions ASME*, 47:335–341.

You, H., Yu, Y., and Kamensky, D. (2020). An asymptotically compatible formulation for local-to-nonlocal coupling problems without overlapping regions. *Computer Methods in Applied Mechanics and Engineering*, 366:113038.

Yu, Y., Bargos, F. F., You, H., Parks, M. L., Bittencourt, M. L., and Karniadakis, G. E. (2018). A partitioned coupling framework for peridynamics and classical theory: analysis and simulations. *Computer Methods in Applied Mechanics and Engineering*, 340:905–931.

Zaccariotto, M., Mudric, T., Tomasi, D., Shojaei, A., and Galvanetto, U. (2018). Coupling of fem meshes with peridynamic grids. *Computer Methods in Applied Mechanics and Engineering*, 330:471–497.

Zaccariotto, M., Shojaei, A., and Galvanetto, U. (2021). Coupling of ccm and pd in a meshless way. In *Peridynamic Modeling, Numerical Techniques, and Applications*, pages 113–138. Elsevier.

Zhao, H., Zhang, L., Wu, Z., and Liu, A. (2022). A new discrete element model for rock-like materials. *Computers & Structures*, 261-262:106730.

Zhu, N., De Meo, D., and Oterkus, E. (2016). Modelling of granular fracture in polycrystalline materials using ordinary state-based peridynamics. *Materials*, 9(12):977.

Zienkiewicz, O. C. and Taylor, R. L. (2005). *The finite element method for solid and structural mechanics*. Elsevier.